Stress-based forecasting of induced seismicity with instantaneous earthquake failure functions: Applications to the Groningen Gas Reservoir.

Jonathan D. Smith[1], Elías R. Heimisson[1,2], Stephen J. Bourne[3], Jean-Philippe Avouac.[1]

Abstract

The Groningen gas field is a natural laboratory to test stress-based forecasting models of induced seismicity due to the detailed knowledge of the reservoir geometry and production history, as well as the availability of surface subsidence measurements and high quality seismicity data. A specific feature of that case example is the exponential rise of seismicity that was detected nearly 30 years after the onset of production. In this study, the subsurface is represented as a homogeneous isotropic linear poroelastic half-space subject to stress changes in three-dimensional space due to reservoir compaction and pore pressure variations. The reservoir is represented with cuboidal strain volumes. Stress changes within and outside the reservoir are calculated using a simple convolution with semi-analytical Green functions. The uniaxial compressibility of the reservoir is spatially variable and constrained with surface subsidence data. Coulomb stress changes are maximum near the top and bottom of the reservoir where the reservoir is offset by faults. To assess earthquake probability, we use the standard Mohr-Coulomb failure criterion assuming instantaneous nucleation and a non-critical initial stress. The distribution of initial strength excess, the difference between the initial Coulomb stress and the critical Coulomb stress at failure,

*Corresponding author: jon$_s$*mith83@hotmail.co.uk*
[1]Division of Geological and Planetary Sciences, California Institute of Technology, Pasadena, 91106, California, USA.
[2]Seismological Service, ETH Zurich, Zurich, Switzerland
[3]Shell Global Solutions, Amsterdam, Netherlands

is treated as a stochastic variable and estimated from the observations. We calculate stress changes since the onset of gas production. The lag and exponential onset of seismicity are well reproduced assuming either a a generalized Pareto distribution of initial strength excess, which can represent the tail of any distribution, or a Gaussian distribution, to describe both the tail and body of the distribution. This representation allows to test if the induced seismicity at Groningen has transitioned to the steady-state where seismicity rate is proportional to the stressing rate. Our results indicate that the system has not yet reached such a steady-state regime. The forecast is robust to uncertainties about the ability of the model to represent accurately the physical processes. It does require in particular a priori knowledge of the faults that can be activated. The method presented here is in principle applicable to induced seismicity in any setting provided deformation and seismicity data are available to calibrate the model.

Keywords: Induced Seismicity, Probabilistic Forecasting, Reservoir Deformation

1. Introduction

The Groningen gas field, situated in the north-east of the Netherlands (Figure 1), has been in production since 1963. Prior to gas extraction, no historical earthquakes had been reported in the area (Dost et al., 2017). Starting in the 1990s small magnitude earthquakes have been detected, with some of these shallow events causing non-structural damage and public concern (Figure 1; Dost et al., 2017). As a result, it was decided to reduce production from 2014 and eventually halt production by 2022 (van der Molen et al., 2019). The concern caused by induced seismicity at Groningen has prompted large efforts to monitor the seismicity and surface deformation induced by the reservoir compaction and to develop quantitative models of the seismicity response to the reservoir operations (e.g. Bourne and Oates, 2017; Bourne et al., 2018; Dempsey and Suckale, 2017; Dost et al., 2017, 2020; Richter et al., 2020).

In this study we take advantage of this dataset to explore different modeling strategies to forecast induced seismicity. We follow the well established paradigm that seismicity is driven by Coulomb stress changes, a view already adopted in previous studies of induced seismicity at Groningen (Bourne and Oates, 2017; Bourne et al., 2018; Dempsey and Suckale, 2017; Richter et al., 2020). We test different strategies to assess stress changes, taking advantage of a refined model of reservoir compaction constrained from production data and from surface deformation measurements (Smith et al., 2019). We additionally assume that the lag of seismicity is due to the fact that faults in this stable tectonic area where not critically stressed initially (Bourne and Oates, 2017; Bourne et al., 2018). Assuming the standard Mohr-Coulomb failure model, an earthquake nucleates when the Coulomb stress on a fault reaches a critical value that represent the fault strength. In this context the seismicity evolution depends on the shape of the function representing the distribution of excess strength, the difference between the initial stress and the critical stress at failure. We test whether the time evolution of seismicity reflects only the tail of that distribution, as assumed in the extreme threshold failure model (Bourne and Oates, 2017; Bourne et al., 2018) which explains well the initial exponential rise of seismicity, or whether it shows a transition to the steady-state regime where seismicity should be proportional to stress rate as assumed for example by Dempsey and Suckale (2017). Dempsey and Suckale (2017) were able to forecast satisfactorily the time-evolution of seismicity assuming such a steady-state regime but didn't model how it was established. In this study, we treat nucleation as an instantaneous response. The nucleation process is in fact not instantaneous and this feature, which can be accounted for using the rate-and-state friction formalism (Dieterich, 1994), could explain the seismicity lag (Candela et al., 2019). We assess the effect of non-instantaneous earthquake nucleation in a follow up (Heimisson et al., 2021) which shows that, although the forecasting performance can been further improved with a more sophisticated representation of earthquake nucleation, the assumption of an instantaneous failure is a appropriate approximation for forecasting seismicity at the annual to multi-annual timescale considered here.

2. Stress changes due to pore pressure variations and reservoir compaction

2.1. Principle of our approach and comparison with previous approaches

To estimate the probability of fault failure, we need to model the stress redistribution due to the reservoir compaction and pore pressure variations within and outside the reservoir with proper account for poroelastic effects (Wang, 2018). The geometry of the reservoir is well known from various geophysical investigations (seismic reflection and seismic refraction), borehole core samples and logging data. The reservoir lies a depth varying between 2.6 and 3.2km, with a thickness increasing northeastward from about 100m to 300m. Numerous faults are offsetting the reservoir (Figure 1) with throws exceeding the reservoir thickness at places. Pressure depletion lead to compaction of the reservoir, shear stress build up on these faults and deformation of the surrounding medium. Various approaches have been used in past studies to calculate the resulting stress redistribution. Some have adopted a simplified model to enable forecasting seismicity at the scale of the entire reservoir as we do in this study. Dempsey and Suckale (2017) proposed a forecasting scheme which accounts for the effect of the local pore pressure change on poroelastic stress changes within the reservoir but ignore the effect of the reservoir non-homogeneous properties. One drawback of this approach is that seismicity tends to occur outside the reservoir in the caprock (Smith et al., 2020), and probably in zones of stress localization induced by spatial variations of the the reservoir properties. Bourne et al. (2018) developed a semi-analytical reservoir depth integrated model which is also limited to the estimate of stress changes within the reservoir itself, but account for stress concentrations at the faults offsetting the reservoir. The faults characteristics are not represented in any detail though. Some other studies have used approaches that allow a more detailed representation of the stress concentration at faults offsetting the reservoir and the assessment of stress changes within and outside the reservoir. In particular, Jansen et al. (2019) used a two-dimensional closed-form analytical expressions to investigate stress redistribution and the possibility of reactivating faults with any geometry. Other authors have carried out similar investigations using two-dimensional finite-element simulations (Mulders, 2003; Rutqvist et al., 2016; Buijze et al., 2017, 2019). These studies provided important insight on the mechanics of fault reactivation, but the methods used to estimate stress redistribution can't be easily included in a seismicity forecasting scheme due to the need to consider 3-D effects and the large scale of the reservoir. Finally some authors have adopted a simplified representation of the deforming reservoir as a series of point sources of strain (van Wees et al., 2019; Candela et al., 2019). This approach is efficient as the Green Functions are analytical. It allows to calculate stress changes in the 3-D volume and can feed a seismicity forecasting scheme easily. It however suffers from the fact that it is very sensitive to the distribution of the point sources representing the reservoir and to the distribution of the receiver points where stress changes are evaluated. This issue is inherent to the point source representation due to the stress singularity at the source location.

In this study, we also use a Green function approach but adopt a strain volume formulation (Kuvshinov, 2008) rather than a point source formulation. The deforming reservoir is represented as a series of cuboidal volumes which are deforming poroelastically. We adopted a cuboidal elementary volumes as it is an efficient way to represent, to the first order, spatial variations of the reservoir geometry, due in particular to the faults offsetting the reservoir. These faults are represented as vertical faults but the method could be expanded to account for any fault dip angles using more general polyhedral elementary volumes. The displacement and stress Green's functions for polyhedral volumes are semi-analytical and therefore easy to compute (Kuvshinov, 2008). This approach has the additional the additional benefit that Green function methods make it easy to compute the stress changes for any production scenario by the convolution of Green's function with the evolving pressure field. This is an appreciable feature for earthquake forecasting, eventually in real-time. A difference between our approach and that of Candela et al. (2019), in addition to the strain volume instead of the point formulation, is that we assume that earthquakes can occur on unmapped faults. We therefore don't restrict the stress calculations to the set of known faults. The advantage is that our approach doesn't require any prior knowledge of the faults that could be reactivated.

2.2. Implementation of the strain-volume model

We use the pressure depletion model developed by the operator (Nederlandse Aardolie Maatschappij, 2013), which was generated from history matching using the production rates, pressure gauge measurements, flow gauge measurements, and tracer timing measurements. The model takes into account the geometry of the reservoir.

Surface subsidence over the gas field has been well documented with different geodetic and remote sensing techniques including optical levelling, persistent scatterer interferometric synthetic aperture radar (PS-InSAR) and continuous GPS (cGPS). Smith et al. (2019) combined all these data to describe the evolution of surface subsidence and the related reservoir compaction from the start of gas production until 2017. They additionally used the pressure depletion model of Nederlandse Aardolie Maatschappij (2013) to determine the spatially variable compressibility of the reservoir. Since the lateral extent of the reservoir ($\sim 40 \times 40km$) is much greater than the reservoir thickness ($100 - 300m$), the reservoir pressure depletion at any map point can be related to the reservoir compaction by:

$$C = C_m \Delta P h \tag{1}$$

where C is the compaction of the reservoir, C_m the uniaxial compressibility, ΔP the pressure depletion and h the reservoir thickness. The uniaxial compressibility was thus determined based on the pressure depletion, the reservoir thickness, and the reservoir compaction (Smith et al., 2019). The semi-analytical Green functions to relate the reservoir compaction to surface subsidence is obtained by the integration of the nucleus of strain solution over the elementary cuboid assumed to be isotropic and homogeneous (Kuvshinov, 2008). The formulation depends on the relative position of the vertices defining each cuboid (i), relative to the observation point, $\vec{x} = (x, y, z)$,

$$\bar{x}_{(i)} = x_{(i)} - x, \tag{2}$$

$$\bar{y}_{(i)} = y_{(i)} - y, \tag{3}$$

$$\zeta^{\pm} = z_{(i)} \mp z, \tag{4}$$

where $x_{(i)}$, $y_{(i)}$ and $\zeta(i)$ are the location for each vertex, with the distance between a vertex and a point in space given by $R^{\pm} = \sqrt{\bar{x}^2 + \bar{y}^2 + (\zeta^{\pm})^2}$. The displacement, $U = (U_x, U_y, U_z)$, at an observation point at the free surface, $Z = 0$, due to a given cuboid is determined from the summation over all its vertices with

$$\begin{aligned} U_x =& \frac{\alpha C_m \Delta P}{4\pi} \sum_{vertices} (-1)^{i-1} \left[f\left(\bar{y}, \zeta_-, \bar{x}, R_-\right) \right. \\ & \left. + (3 - 4\nu) f\left(\bar{y}, \zeta_+, \bar{x}, R_+\right) + 2 \cdot z\log\left(|R_+ \bar{y}|\right) \right], \end{aligned} \tag{5}$$

$$\begin{aligned} U_y =& \frac{\alpha C_m \Delta P}{4\pi} \sum_{vertices} (-1)^{i-1} \left[f\left(\bar{x}, \zeta_-, \bar{y}, R_-\right) \right. \\ & \left. + (3 - 4\nu) f\left(\bar{x}, \zeta_+, \bar{y}, R_+\right) + 2z \cdot \log\left(|R_+ + \bar{x}|\right) \right], \end{aligned} \tag{6}$$

$$\begin{aligned} U_z =& - \frac{\alpha C_m \Delta P}{4\pi} \sum_{vertices} (-1)^{i-1} \left[f\left(\bar{x}, \bar{y}, \zeta_-, R_-\right) \right. \\ & \left. + (3 - 4\nu) f\left(\bar{x}, \bar{y}, \zeta_+, R_+\right) - 2z \cdot \mathrm{atan}\left(\frac{\zeta_+ R_+}{\bar{x}\bar{y}}\right) \right], \end{aligned} \tag{7}$$

where the function f is defined,

$$f\left(x, y, Z, R\right) = Z \cdot \mathrm{atan}\left(\frac{xy}{ZR}\right) - x\ln\left(|R + y|\right) - y\ln\left(|R + x|\right). \tag{8}$$

Following Smith et al. (2019) we represent the reservoir with cuboids having a X-Y dimension size equal to $500m \times 500m$. The depth and height of each cuboid is set to the average depth and thickness of the reservoir over this $500 \times 500m$ area.

Smith et al. (2019) found that the uniaxial compressibility is pressure invariant but spatially heterogeneous (as shown in Figure 8 of Smith et al. (2019)) with a resolution approximately equal to the $3km$ depth of the reservoir. As such the uniaxial compressibility model represents a smoothed representation of the reservoir compressibility. Downstream applications of this model for stress calculations, Coulomb stress and earthquake forecasting should be smoothed to the same $3km$ resolution.

The depth distribution of hypocenters which were relocated by Smith et al. (2020), with a depth uncertainty of $500m$, suggests that earthquake nucleate within the reservoir (28%) or in the overburden (60%), with the mode of the distribution peaking in the reservoir caprock. Therefore stress changes are evaluated both within, and outside, the reservoir. We assume no pore pressure depletion outside the reservoir.

The stress changes are calculated with Kuvshinov (2008) solution,

$$\begin{aligned}\sigma_{xx} =& \frac{\alpha C_m G \Delta P}{2\pi} \sum_{vertices} (-1)^{i-1} [-\mathrm{atan}\left(\frac{\bar{x}R_-}{\bar{y}\zeta_-}\right) - (3-4\nu)\,\mathrm{atan}\left(\frac{\bar{x}R_+}{\bar{y}\zeta_+}\right) \\ &+ 4\nu \cdot \mathrm{atan}\left(\frac{\zeta_+ R_+}{\bar{x}\bar{y}}\right) - \frac{2\bar{x}\bar{y}z}{R_+\left(\bar{x}^2+\zeta_+^2\right)}],\end{aligned} \tag{9}$$

$$\begin{aligned}\sigma_{yy} =& \frac{\alpha C_m G \Delta P}{2\pi} \sum_{vertices} (-1)^{i-1} [-\mathrm{atan}\left(\frac{\bar{y}R_-}{\bar{x}\zeta_-}\right) - (3-4\nu)\,\mathrm{atan}\left(\frac{\bar{y}R_+}{\bar{x}\zeta_+}\right) \\ &+ 4\nu \cdot \mathrm{atan}\left(\frac{\zeta_+ R_+}{\bar{x}\bar{y}}\right) - \frac{2\bar{x}\bar{y}z}{R_+\left(\bar{y}^2+\zeta_+^2\right)}],\end{aligned} \tag{10}$$

$$\begin{aligned}\sigma_{zz} =& -\frac{\alpha C_m G \Delta P}{2\pi} \sum_{vertices} (-1)^{i-1} [-\mathrm{atan}\left(\frac{\zeta_- R_-}{\bar{x}\bar{y}}\right) + \mathrm{atan}\left(\frac{\zeta_+ R_+}{\bar{x}\bar{y}}\right) \\ &+ \frac{2\bar{x}\bar{y}z}{R_+}\left(\frac{1}{\bar{x}^2+\zeta_+^2} + \frac{1}{\bar{y}^2+\zeta_+^2}\right)],\end{aligned} \tag{11}$$

$$\begin{aligned}\sigma_{xy} =& -\frac{\alpha C_m G \Delta P}{2\pi} \sum_{vertices} (-1)^{i-1} [\ln\left(|R_- + \zeta_-|\right) \\ &+ (3-4\nu)\ln\left(|R_+ + \zeta_+|\right) - \frac{2z}{R_+}],\end{aligned} \tag{12}$$

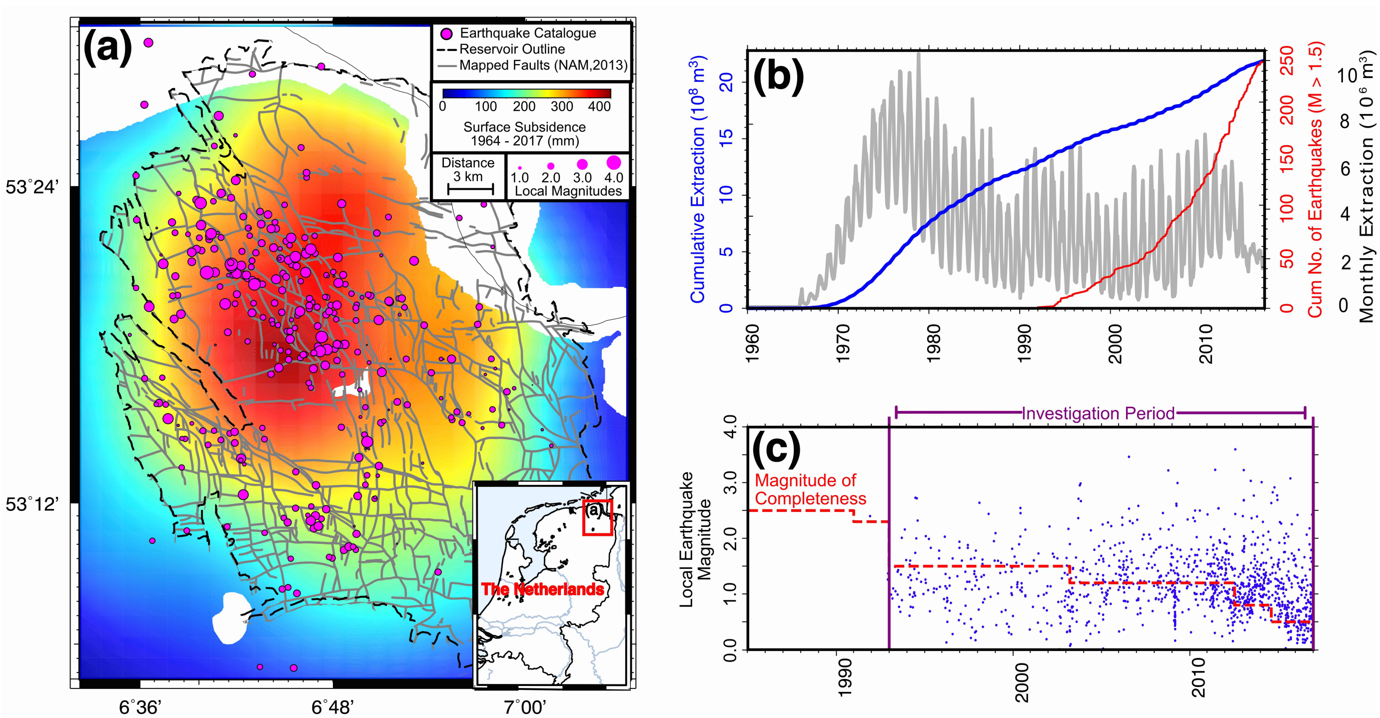

Figure 1: Relationships between surface subsidence, seismicity and cumulative extraction. (a) Modelled surface subsidence between 1964-2017. Seismicity between 1964-2017 shown by pink circles with size scaled by magnitude (Maximum Magnitude $M_L = 3.6$). Gas extent within the reservoir shown with black dashed outline. Mapped faults shown by grey line. (b) Time evolution of the cumulative extraction, monthly extraction, and cumulative number of earthquakes. (c) Earthquake magnitude variation from 1985-2017. Red dashed line show magnitude of completeness. Blue circles the observed seismicity. Purple lines show the time period under investigation in this article.

$$\sigma_{xz} = \frac{\alpha C_m G \Delta P}{2\pi} \sum_{vertices} (-1)^{i-1} [\ln\left(\left|\frac{R_- + \bar{y}}{R_+ + \bar{y}}\right|\right) - \frac{2z\bar{y}\zeta_+}{R_+\left(\bar{x}^2 + \zeta_p^2\right)}], \tag{13}$$

$$\sigma_{yz} = -\frac{\alpha C_m G \Delta P}{2\pi} \sum_{vertices} (-1)^{i-1} [\ln\left(\left|\frac{R_- + \bar{x}}{R_+ + \bar{x}}\right|\right) - \frac{2z\bar{x}\zeta_+}{R_+\left(\bar{y}^2 + \zeta_p^2\right)}]. \tag{14}$$

In our calculations, the Biot's coefficient is set to $\alpha = 1.0$ and the Poisson ratio to $\nu = 0.25$. The displacement and stress fields for a single cuboid is shown in Supplementary Figure A1. The cross-section is taken along the y-axis in the centre of the cuboid. Note the stress localization at the edges of the cuboid. The free surface has little effect in he case of a single cuboid due to its small size compared to the reservoir depth.

A cross-section of the displacement and stress calculated with our representation of the reservoir as a series of cuboids is shown in Figure 2. The figure also shows the maximum Coulomb stress changes and a 'fault Coulomb stress' change calculated on faults orientated parallel to the regional average (Strike=270^o, Dip=85^o; Nederlandse Aardolie Maatschappij, 2013). The cross-section is composed of 8174 receiver points at 15m spacing in X and Z dimensions, computed from the convolution with the 8174 cuboids. The calculation takes 60s with the code supplied in the Google Colab notebook. In addition, across the continuous reservoir the stress concentrations at the edges of individual cuboids interfere destructively. The Coulomb stress changes are largest at the top or bottom of the reservoir in the vicinity of the most prominent reservoir discontinuities. To show how the maximum Coulomb stress change attenuates away from this zone of stress localization we show depth slices taken at various elevation above, within or below the reservoir. The stress changes are calculated on a $500 \times 500m$ grid of points that coincide in map view with the centers of the cuboids. We also show the smoothed stress field (using a Gaussian kernel with 3.2km standard deviation to account for the resolution of spatial variations of compressibility) which is used as an input for earthquake forecasting. Within the reservoir, the the pore pressure decrease outweighs the increase of the horizontal stresses due to poroelasticity, leading to a decreasing of Coulomb stress (Figure 2). However, both above and below the reservoir in the region that is pressure isolated to the reservoir, the Coulomb stress shows a positive increase with comparable spatial features above a below the reservoir. As you move further away from the reservoir top interface to shallower depths you see a decrease in the amplitude of the Coulomb stress with a spatial feature changing from a Coulomb stress high in the south-west of the reservoir to the north-east, but with little variation within the top $50m$ of the reservoir (Figure 3 and Supplementary Figure A2). The Coulomb stress changes calculated for faults with orientation parallel to regional average are very similar (see Supplementary Figure A3).

Given that the depth distribution of hypocenters peaks right above the top of the reservoir, we estimate seismicity rate based on the maximum Coulomb stress change computed $5m$ above the top of the reservoir with the strain-volume model (Figure 4b; with forecasting potential at different depth slices and different Coulomb models discussed further in Section 3). In addition, slices from the time-evolution of the maximum Coulomb stress $5m$ above the reservoir can be found in Supplementary Figure A4.

2.3. Comparison with other models of stress redistribution

We compare our results with the stress change calculations presented by Candela et al. (2019) and to those obtained with the Elastic Thin-Sheet (ETS) approximation of Bourne and Oates (2017).

The comparison with the Coulomb stress changes presented in Candela et al. (2019) show an overall similar pattern, with larger stress changes in area or larger subsidence, but the differences are locally large (Figure 5). Even in absence of any smoothing our model yields a much smoother stress field. The chief reason is that Candela et al. (2019) resolved the stress changes only on a set of known faults. In addition, we sample the stress field at points coinciding in map view with the centers of the cuboids. As a result we don't sample the larger

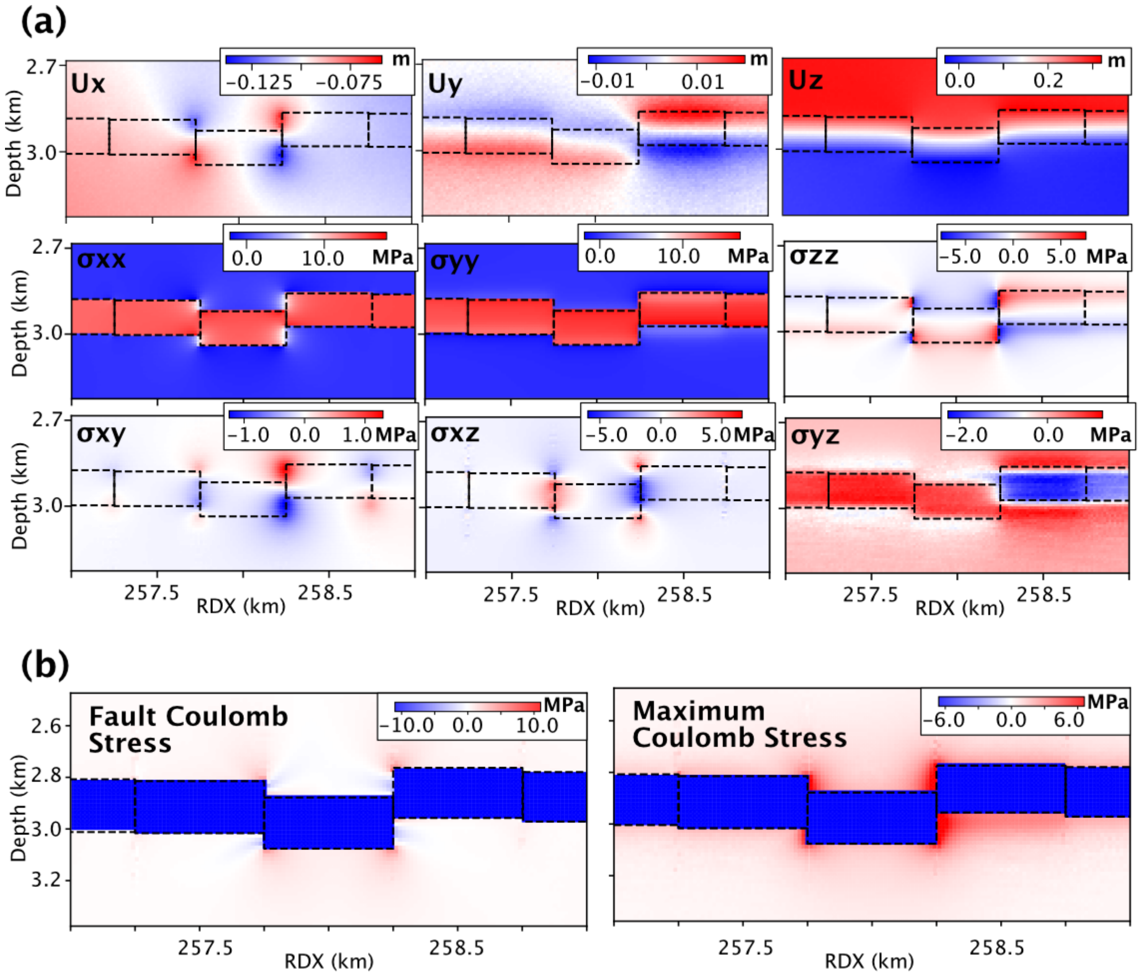

Figure 2: (a) Displacement (U in m), and stress tensor components (σ in MPa) along a vertical cross-section through a series of cuboids representing the simplified geometry of the depleting reservoir (black dashed lines). (b) Maximum Coulomb stress and fault Coulomb stress (MPa) calculated for a fault orientation corresponding to the regional average strike (270^o), and dip (85^o) angles.

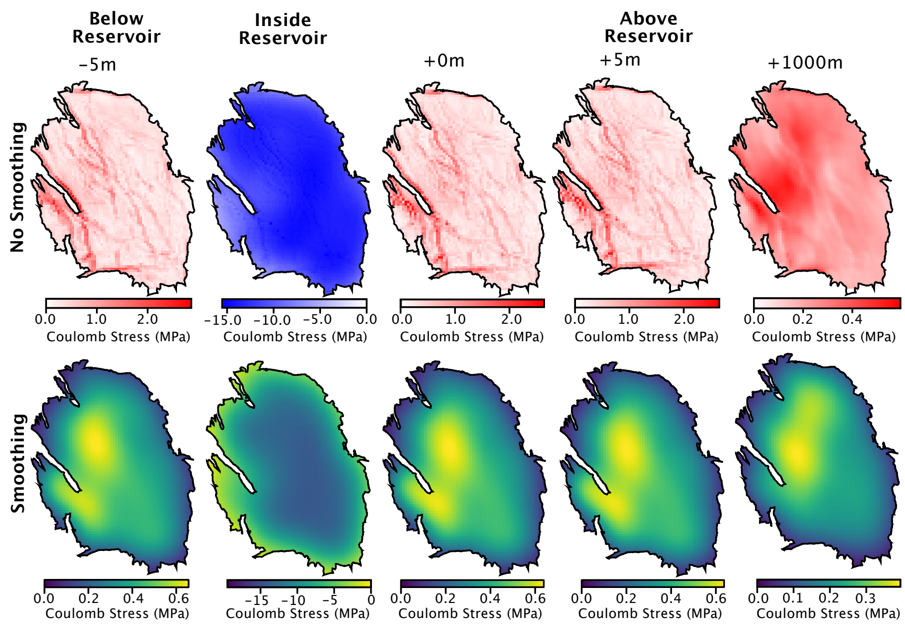

Figure 3: Maximum Coulomb stress changes from 1965 to 2017 at various elevations relative to the reservoir. (a)-(e) represent the maximum Coulomb stress for the unsmoothed. (f)-(j) maximum Coulomb stress models smoothed to a length scale consistent with uniaxial compressibility ($3.2km$).

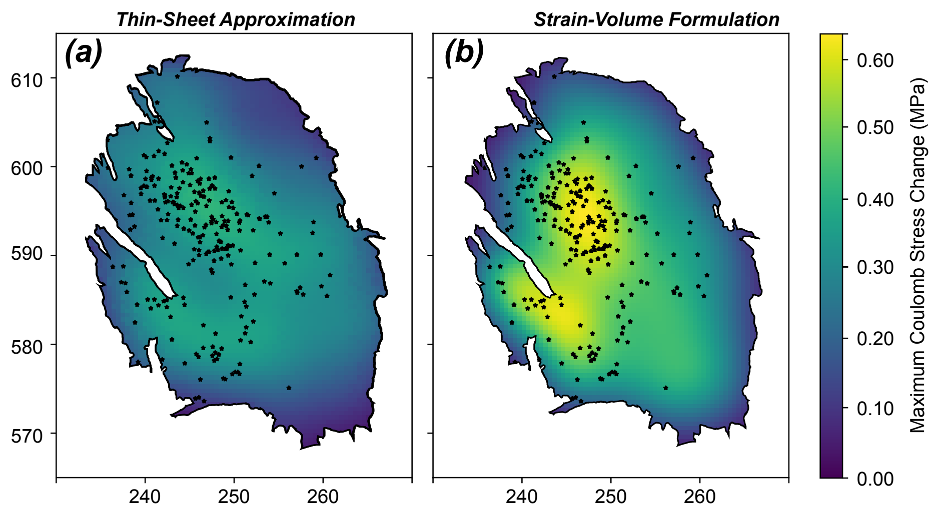

Figure 4: Comparison of the Thin-Sheet Bourne and Oates (2017) and Strain-Volume maximum Coulomb stress change for the period of 1965-2017. (a) Thin-sheet maximum Coulomb stress change with black outline representing the reservoir outline at depth and red dots the observed earthquake locations. (b) Strain volume maximum Coulomb stress change calculated 5 m above the top of the reservoir.

stress values at the junctions between the cuboids. Neither model is completely satisfying to yield a realistic estimate of the stress field at the exact location of where the earthquakes are induced.

In the ETS formulation, the vertical averaged strain of a reservoir with spatially varying thickness $h(x, y)$ is expressed a function of the vertical strain, ε_{zz} and reservoir depth, z_0 according to,

$$\bar{\varepsilon}_{xz} = -\frac{\varepsilon_{zz}}{2}\frac{\partial z_0}{\partial x} + \frac{h}{4}\frac{\partial \varepsilon_{zz}}{\partial x}, \tag{15}$$

$$\bar{\varepsilon}_{yz} = -\frac{\varepsilon_{zz}}{2}\frac{\partial z_0}{\partial y} + \frac{h}{4}\frac{\partial \varepsilon_{zz}}{\partial y}, \tag{16}$$

$$\bar{\varepsilon}_{zz} = \varepsilon_{zz}. \tag{17}$$

The ETS formulation approximates the reservoir deformation as a uniaxial vertical strain field, with zero horizontal strain, and does not describe the asso-

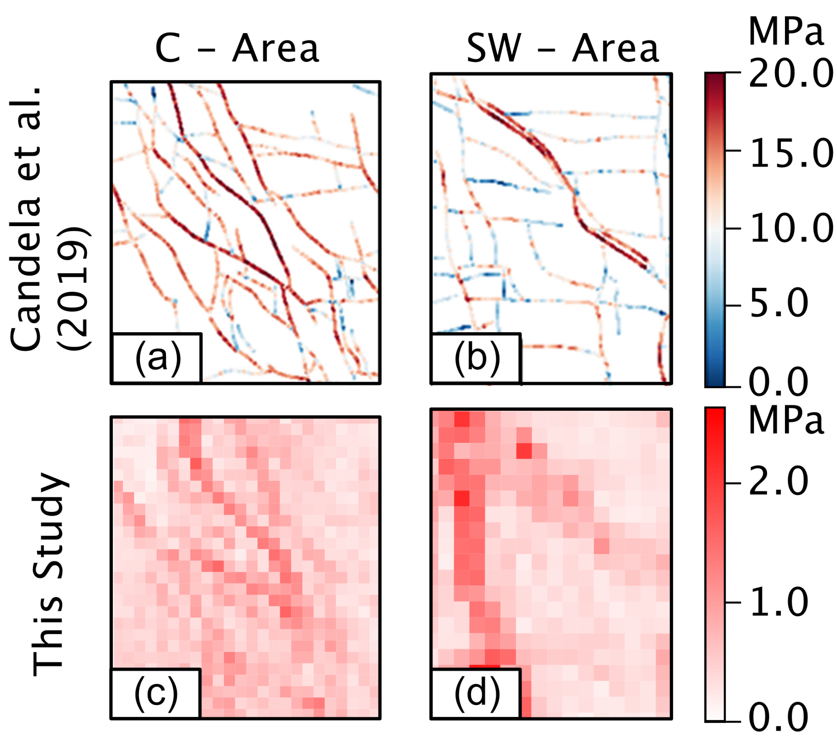

Figure 5: Coulomb stress comparison between this studies maximum Coulomb stress and Candela et al. (2019) at start of 2016. The regions South-West (SW-area) and Central (C-Area) are outlined further Candela et al. (2019).

ciated caprock deformation. In their implementation Bourne and Oates (2017) apply a spatial smoothing and filter out faults with offset exceeding some given fraction of the reservoir thickness offset. The two parameters, optimized to best fit the seismicity data using a Markov-Chain Monte Carlo procedure, were determined as $3.2km$ and 0.43 respectively. The spatial smoothing is consistent with the resolution of spatial variations of compaction due to the $3km$ depth of the reservoir. The rationale to justify thresholding faults with large offset relative to the reservoir thickness is the presence of possible aseismic salt formation above the anhydrite caprock. Faults with large offset juxtapose the reservoir against the salt and could be considered aseismic.

We compare the maximum Coulomb stress change across $1965 - 2017$ for the thin-Sheet formulation (Bourne and Oates, 2017) and maximum Coulomb stress of the strain-volume $5m$ above the reservoir but external to the pressure communication (Figure 4), as the Coulomb stress within the reservoir is stable at all of our observation points with negative Coulomb stress values. Although the two stress calculation methods significantly differ, the spatial motif of the Coulomb stress values are similar with only differences in the magnitude of the Coulomb stress values. In the forecasting procedure these differences will be incorporated in the parameter definitions, with similar forecasts given for the different stress calculations.

3. Relating stress changes and seismicity

Stress-based earthquake forecasting requires some scheme to relate induced seismicity to stress changes. Previous Earthquake forecasting studies focused on Groningen have assumed instantaneous failure and a non-critical initial stress (Bourne and Oates, 2017; Bourne et al., 2018; Dempsey and Suckale, 2017), or non-instantaneous failure based on rate-and-state friction (Candela et al., 2019; Richter et al., 2020). In this study we aim at simulating the evolution of seismicity at the annual to multi-annual timescale. In a related study we show that the finite duration of earthquake nucleation doesn't matter at these time scales (Heimisson et al., 2021). We therefore assume here instantaneous failure. Below we test the possibility that the seismicity is consistent the near-exponential rise of seismicity rate due to the tail of the distribution, represented by a generalized Pareto distribution by Bourne et al. (2018), or has transitioned to the steady regime assumed by Dempsey and Suckale (2017).

The point of failure of an intact rock or of reactivation of an existing fault is commonly assessed using the Mohr-Coulomb failure criterion (Handin, 1969). A number of studies have also demonstrated that this criterion can be used effectively to assess earthquake triggering by stress changes (e.g. King et al., 1994). According to this criterion failure occurs when the shear-stress τ exceeds the shear-strength of the material τ_f, represented by

$$\tau_f = \mu(\sigma_n - P) + C_0, \tag{18}$$

where τ_f is shear-stress, σ_n is the normal-stress (positive in compression), P is the pore pressure, μ is the internal friction and C_0 is the cohesive strength. If the material is not at failure the strength excess is $\tau_f - \tau$. Pressure changes play an important role in preventing or promoting fault failure. Assuming the total stresses do not change, a greater pore pressure acts to lower the effective normal stress and promotes failure. By contrast, a pressure decrease should inhibit failure. It is customary to assess jointly the effect of stress changes and pore pressure changes using the Coulomb stress change defined as

$$\Delta C = \Delta\tau + \mu(\Delta\sigma_m + \Delta P), \tag{19}$$

where ΔC is the change in Coulomb stress, $\Delta\tau$ is the shear stress change, μ is the internal friction, $\Delta\sigma_m$ is the change in normal stress, and ΔP is the change in pore pressure.

It is in principle possible to use our model and the observed seismicity to estimate the initial strength excess, representing the Coulomb stress change needed to bring a fault patch to failure. An earthquake indicates a Coulomb stress change due to gas production equal to the initial strength excess before production started. This calculation requires some knowledge of the fault orientation, which is known only for a very limited number of earthquakes for which focal mechanisms could be calculated (Smith et al., 2020). Therefore, we make the calculation for the fault orientation that yields the maximum Coulomb stress change or the regional fault orientation. This distribution does not rigorously represent the strength excess, but can be considered a proxy for it, which we use to estimate of probability of inducing an earthquake at a given stress change ΔC_m. In fact, we can only estimate the part of the initial strength distribution that is revealed by seismicity. Any forecast requires a parametric representation of the part of the distribution that has not yet been brought to failure. The shape of that distribution depends in principle on the orientation of the faults and the heterogeneities of the effective stress tensor. For a homogenous triaxial stress regime and standard Mohr-Coulomb failure criterion, the strength excess can be calculated assuming some distribution of fault orientations. If the activated faults have all the same orientation either because they correspond to a pre-existing tectonic fabric, or are optimally oriented with respect to the stress field, the distributions should be close to a Dirac distribution. In that case all earthquakes would happened at approximately the same Coulomb stress change. Our calculation shows a relatively wide spread of values. The spread of this distribution can result from the heterogeneities of initial effective stress, cohesion, friction, fault orientation, hypocentral depths and from the uncertainties in the stress change calculation. We therefore consider the strength excess as a stochastic variable. This approach is similar to the Extreme threshold Model of (Bourne and Oates, 2017; Bourne et al., 2018) which assumes that the seismicity only reflects the tail of the failure probability function (failure of the faults with the smallest strength excess). According to the extreme value theory the tail of the distribution can be represented by a generalised Pareto distribution (Figure 6) so that the failure probability function becomes

$$P_f = \exp(\theta_1 + \theta_2 \Delta C), \tag{20}$$

where $\theta_1 = \frac{C_t}{\bar{\sigma}}$ and $\theta_2 = \frac{1}{\bar{\sigma}}$ relate to the mean C_t , and standard-deviation $\bar{\sigma}$ of the initial strength excess distribution.

However, it is possible that the seismicity may have transitioned to a more steady regime in which case the representation of only the tail of the distribution might be inadequate. For each fault the distribution of strength excess depends on the probability distributions describing its orientation, stress and strength. Heterogeneities of stress resulting from variations of elastic properties of lithological origin can result in a Gaussian distribution of Coulomb stress changes (Langenbruch and Shapiro, 2014). The other factors of strength excess variability might be assumed, like the geometric effect due to the faults orientation, to be unimodal as well. If we assume that the initial Coulomb stress values on different fault patches are independent and identically distributed random values, then, by virtue of the central limit theorem, we may assume a Gaussian distribution of initial strength excess, as is expected in the case where the only source of strength excess is due to heterogeneities of elastic properties (Langenbruch and Shapiro, 2014). In that case the probability of failure of a fault at a location with a maximum Coulomb stress changes ΔC is derived from integration of the Gaussian function yielding

$$P_f = \frac{1}{2}\left(1 + \mathrm{erf}\left(\frac{\Delta C - \theta_1}{\theta_2\sqrt{2}}\right)\right), \tag{21}$$

where θ_1, θ_2 represent the mean and standard deviation of the Gaussian distribution, representing the fault strength distribution. This formulation is shown by the blue line in Figure 6b, with the initial Gaussian represented by the dashed blue line. As the Coulomb stress increases, the first earthquakes will occur on the faults with the lowest strength excess and so will provide information on the tail of the initial strength excess distribution. In that regime the extreme value theory implies an exponential rise of seismicity for a constant stress rate (Bourne and Oates, 2017). As the stress increases to a value of the order of the mean initial strength excess (θ_1) the seismicity rate will gradually evolve to a regime where the seismicity rate will be proportional to the stress rate. If the faults that have already ruptured are allowed to re-rupture and if the Coulomb

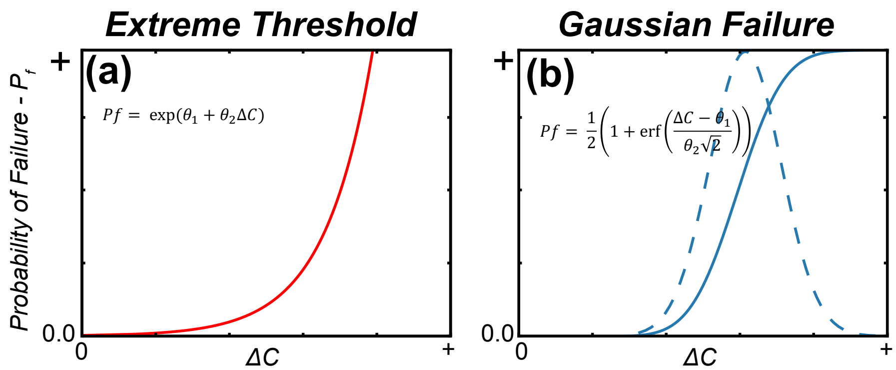

Figure 6: Probabilistic failure functions for a Extreme-Threshold or Gaussian Failure. (a) Extreme threshold. (b) Gaussian Failure function with the blue dashed line representing the Gaussian distribution and the solid dashed line the cumulative distribution function.

stress has increased to a value significantly larger than the typical stress drop during an earthquake, the distribution of strength excess will become uniform (constant between 0 and the co-seismic stress drop); the seismicity rate would then remain proportional to the stress rate. This is the steady regime expected an active tectonic setting for instantaneous nucleation (Ader et al., 2014). One important question for seismic hazard assessment at Groningen is whether the system has moved out of the initial exponential rise of seismicity. To address this question, we compare the performance of the Gaussian model describes above, which allows for this transition, and of the Extreme threshold Model of Bourne and Oates (2017) which assumes that the seismicity only reflects the tail of the failure probability function.

4. Estimation of model parameters

We use an optimisation scheme to determine the best fitting failure function parameters relating the modelled Coulomb stress change with the observed

Failure Function	θ_1 Bounds	θ_2 Bounds	θ_3 Bounds
Extreme Threshold	$0.0 - 15.0$	$0.0 - 30.0$	$0.0 - 2.0$
Gaussian Failure	$0.01 - 0.75$	$0.01 - 0.75$	$-2.0 - 15$

Table 1: Failure function uniform priors for Extreme Threshold and Gaussian Failure functions.

regional seismicity. We use the catalogue of Dost et al. (2017) which reports earthquake locations since 1990, with a completeness of $M_{LN} > 1.5$ since 1993. We separate the observed earthquakes into yearly bins, denoted as R^o_y, where subscript y indicates the year and superscript ^{o} stands for "observed". We select a training period $y \in [y_s : y_e]$, where y_s represents the start year of training and y_e is the end year bin. The start year is selected as $y_s = 1990$, where the magnitude of detection is consistently above $M_{LN} = 1.5$ (Dost et al., 2017). The end year is set at 2012 and $2012 - 2017$ is used for validation. The bounds of the uniform prior for the parameter optimisation for the Extreme Threshold and Gaussian failure functions are given in Table 1.

Predicted earthquake rates are formulated using a Poisson point process with the intensity function represented by:

$$\Lambda = \theta_3 \frac{\partial P_f}{\partial t} \tag{22}$$

where λ represents an earthquake productivity per given volume and $\frac{\partial P_f}{\partial t}$ the partial differential of the probability function changing in time. This formulation contains three unknowns, θ_1, θ_2 and θ_3, which are assumed spatially constant across the reservoir.

For parameter optimisation we use the log-likelihood functions

$$\log(p(m|R^o)) = -\frac{1}{2} \sum_i \left(\frac{R^o_i - R^p(m, t_i)}{\sigma} \right)^2 - \sum_i \log\left(\sqrt{2\pi}\sigma\right) + \log(p(m)), \tag{23}$$

where $m = m_1, m_2, \ldots$ is the set of model parameters, $R^o = R^o_{y_s}, R^o_{y_s+1}, \ldots R^o_{y_e}$ is the set of observed seismicity rate. $R^p(m, t_i)$ is the model predicted seismicity rate evaluated at times $t_i = y_s + 1/2, y_s + 3/2, \ldots y_e + 1/2$ evaluated at the center of each time-bin. $p(m)$ is the prior probability distribution, which is taken as uniform for each model parameter. The log-likelihood is thus derived from Bayes theorem where the probability of the observed seismicity rate given the model ($p(R^o|m)$) is taken to be represented by Gaussian probability distribution with a standard deviation σ for each model value. Here we have taken $\sigma = 1$ events/year. This value is justified assuming that $R^o_y \approx \mu$ where μ the rate parameter of a stationary Poisson process that produced events during year bin y. Further, the mean of the Poisson distribution is also μ and the standard deviation is $\sigma_p = \sqrt{\mu}$. Note that $R^o_y = N^o_y/\Delta t$, where N^o_y is the number of events in bin y and Δt is the length of the bin, that is $\Delta t = 1$ year. If the central limit theorem hold the sample mean R^o_y can be considered a normally distributed quantity and the standard deviation of the sample mean is $\sigma = \sqrt{\mu}/\sqrt{N^o_y} \approx \sqrt{R^o_y}/\sqrt{N^o_y} = 1/\Delta t = 1$ events/year. While some bins may not contain sufficient number of events to appeal to the central limit theorem, we find that this simple characterization of the variance produces samples that in a good agreement with the validation.

We quantify misfit using a Gaussian log-likelihood function

$$\log(p(m|R^o)) = -\frac{1}{2} \sum_{i=1990}^{i=2016} \left(R^o_i - \int_{\Sigma} R(m, i, x, y) dxdy \right)^2, \tag{24}$$

where $R(m, i)$ is the model predicted rate density in year i, where m is the vector of model parameters. R^o_i is the observed rate in year i. Integration in Easting, x, and Northing y, is carried over the area Σ. In the Gaussian log-likelihood function we assumed that the standard deviation of the observed seismicity rate is 1 event/year, which is why the weighting each term by a variance is omitted in Equation 24. We opted for a Gaussian log-likelihood function over the a Poissonian log-likelihood Ogata (1998) because of the predicted seismicity rate can be equal to zero ($R = 0$). In this case the Poissonian log-likelihood would assign a zero probability to the tested model that has a zero earthquake rate for any given year, making the Poissonian log-likelihood unfeasible for simulations with a stress threshold. During the training we sample the PDF (Equation 24) using an Metropolis-Hastings sampler. After sufficient number of samples, hindcasts are obtained by selecting 1000 random samples of $m = m_1, m_2, \ldots$ at random and computing $R^p(m,t)$ for $t > y_e + 1$.

5. Results

5.1. Failure Functions and temporal evolution of seismicity

We compare the observed earthquake catalogue with synthetic catalogs simulated using the stress change calculated with strain-volume formulation for the Gaussian and Extreme-Threshold failure functions. To simplify the forecast we assume that earthquakes nucleate within the reservoir caprock and therefore relate the seismicity to stress changes calculated $5m$ above the reservoir top. We test below that the forecast is insensitive to the choice of this particular depth slice. The observed time-evolution of seismicity is compared to the prediction for the Gaussian and Extreme-Threshold models in Figures 7a and 7c respectively. We also compare the observed and predicted maximum expected magnitudes in Figures 7b and 7d. The predicted maximum expected magnitude is calculated for a given population of events with the magnitude given by a pure power-law distribution assuming a non-truncated Gutenberg-Richter distribution,

$$M_{max} = M_c + \frac{1}{b}\log_{10}(N) \tag{25}$$

where b is the slope of the power law, M_c is the reference magnitude and N is the number of earthquakes above the reference magnitude M_c. Note that the predicted mean curve is rather smooth but while the curves corresponding to individual synthetic catalogs show a limited number of steps as seen in the real catalogue.

The differences between the earthquake rates derived from the extreme-threshold and Gaussian failure model are insignificant over the training period. However, we note that the Gaussian model predicts a longer seismicity lag with the onset of seismicity occurring three years after that of the extreme-threshold (Figure 7a and 7b). The synthetic maximum magnitudes are similar between the two formulations, with the Gaussian formulation consistently lower than the magnitude of completeness prior to the 1990s due to the later onset of seismicity. As a result the extreme-threshold model tend to predict a larger cumulative number of earthquakes and therefore larger expected maximum magnitudes than the Gaussian model which also overpredicts but fits the observations slightly better. Figure 7d shows that the assumption of a constant b-value tend to slightly over-predict the maximum magnitude suggesting the possibility of a variable b-value. The fit to the expected maximum magnitude obtained with our strain-volume calculation could similarly be improved by allowing for a variable b-value, with initially lower values as proposed by Bourne and Oates (2017). Figure 8 shows the distribution of Coulomb stress changes calculated at the earthquake location for comparison with the failure functions obtained from our inversion. The comparison shows that even with the Gaussian model the seismicity data constrain mostly the tail of the distribution. Some of the acceptable Gaussian models show a roll-over that would suggest the beginning of the transition to a more steady regime. In any case, the two model parameterizations yield relatively similar failure function in the domain constrained by the observations.

Investigating the temporal forecasting potential across all the Coulomb stress depths and using either the maximum Coulomb stress change or the Coulomb stress change calculated for the average fault orientatioon, we find little variation in the training logp value. All models preform similarly. However the model parameters of the different best fitting models can be significantly different depending on these choices. The validation logp is best for the forecast based on the Coulomb stress change calculated $5m$ above the reservoir (Supplementary Figures A5 and A6).

5.2. Spatial distribution of seismicity

We compare here the spatial distribution of earthquake probability predicted by our models to the observed seismicity. We test the strain-volume and thin-sheet stress redistribution models, and the extreme-threshold and Gaus-

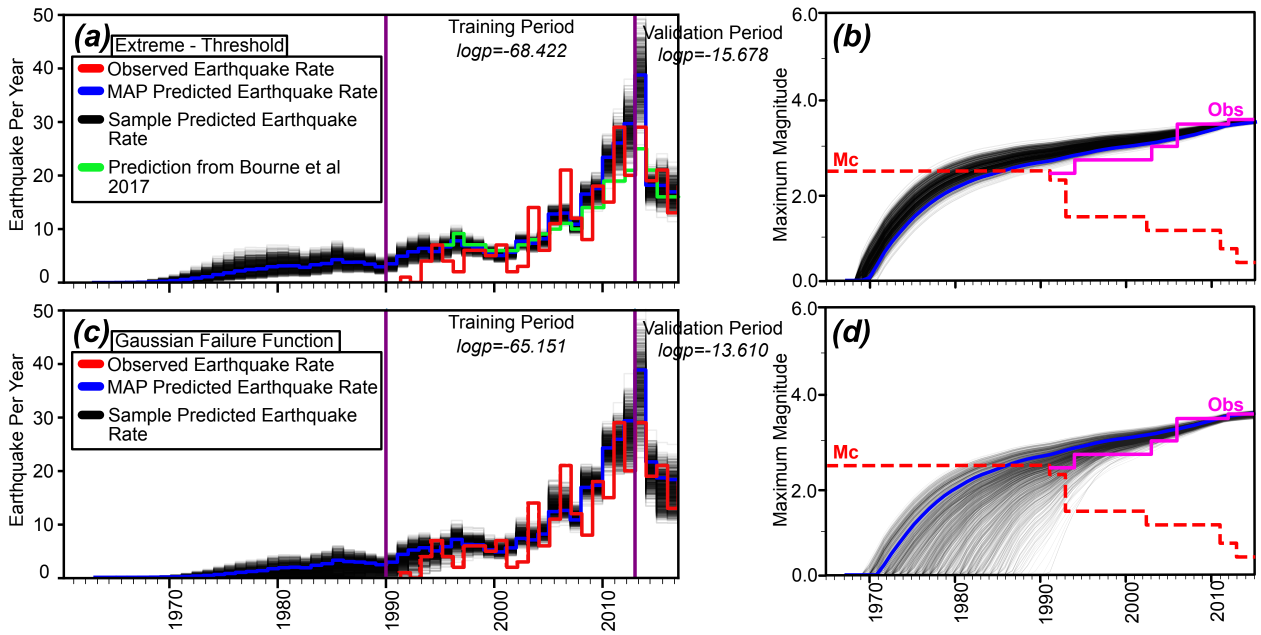

Figure 7: Comparisons of the observed catalogue with the synthetic catalogues generated for the extreme-threshold (a) and Gaussian (b) failure models using the strain-volume formulation. Left panels show seismicity rate and right panel the maximum magnitude since the onset of gas production. Blue lines represent the maximum posterior estimate of synthetic earthquake rate. Black lines represent samples from the probability distribution with colour dependent on the probability. Red solid line represents the observed seismicity catalogue used for training. Pink dashed line represents the magnitude of completeness of the seismicity catalogue. The green line in left panel (a) represents the maximum posterior estimate of the best fitting solution from Bourne and Oates (2017). The orange ticks in left panels mark the onset of seismicity according to the best-fitting extreme-threshold model.

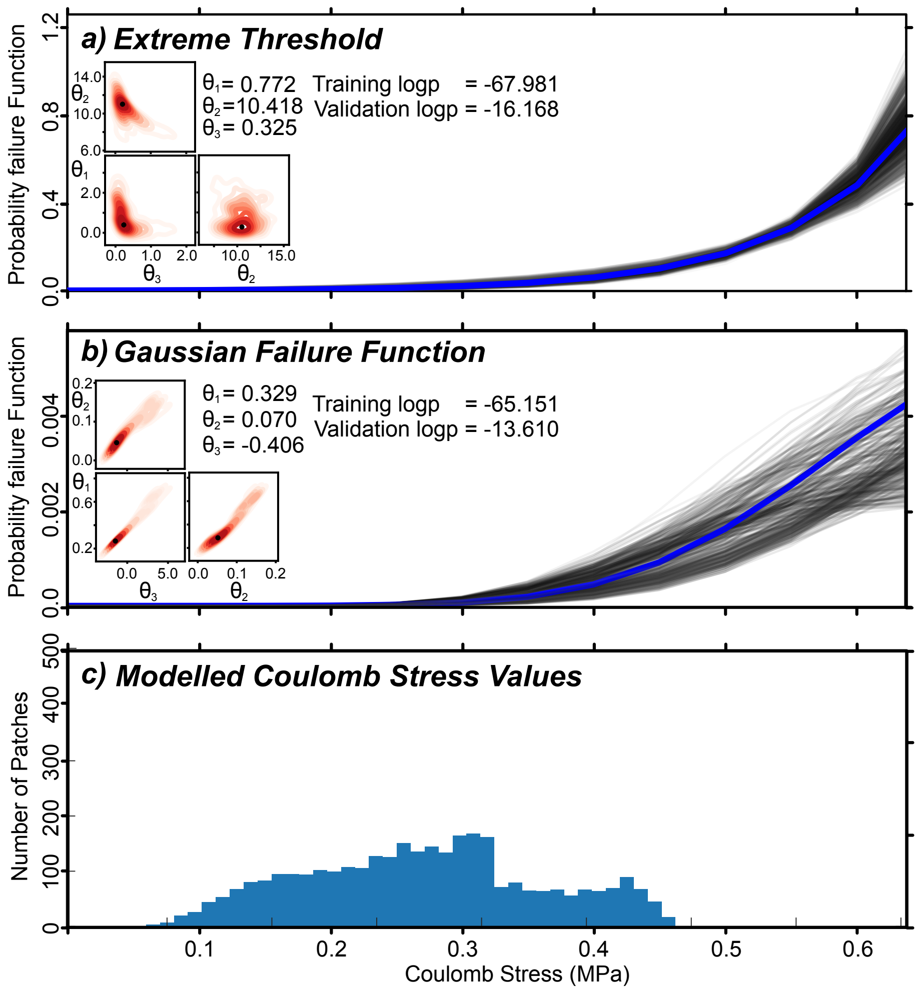

Figure 8: Optimised probability failure functions for the extreme-threshold and Gaussian failure functions. Blue lines represent the maximum a priori estimate of synthetic earthquake rate. Black lines represent samples from the probability distribution with colour dependent on the probability. (a) Extreme threshold failure function. (b) Gaussian failure function. (c) Histogram of the modelled Coulomb stress values across the reservoir from the strain-volume formulation.

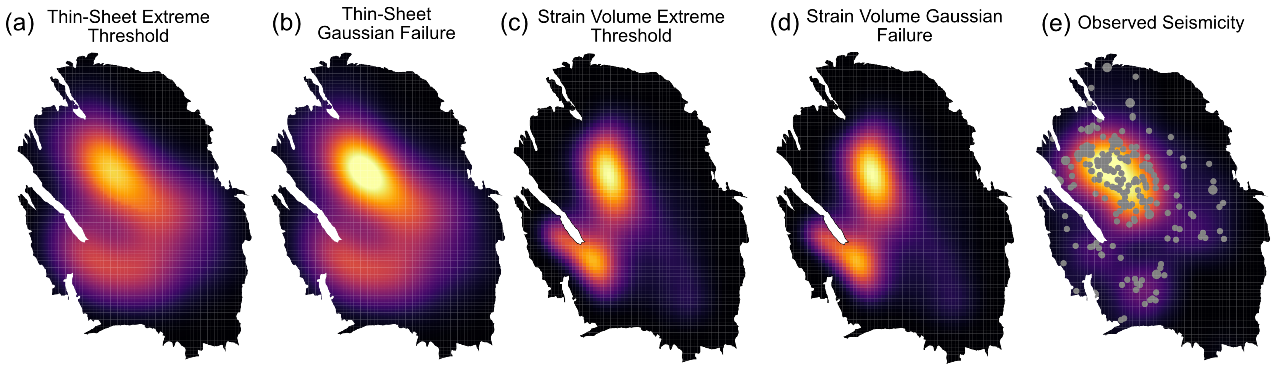

Figure 9: Spatial distribution for the probability failure function for each of the synthetic catalogues and comparison with wit the observed seismicity catalogue spanning $1993 - 2012$. (a) Thin-sheet formulation using extreme threshold failure criterion. (b) Thin-sheet stress formulation using Gaussian failure function. (c) Strain volume using the extreme threshold failure function. (d) Strain volume using the Gaussian failure function. (e) Observed seismicity catalogue shown by white dots, with colourmap showing the probability of failure smoothed to the same length scale of 3.2 km

sian failure models, leading to four synthetic simulations catalogues spanning $1990 - 2017$. Figure 9 represents the comparison of these four synthetic seismicity simulations and the observed seismicity catalogue with a $3.2km$ Gaussian smoothing applied to the observed seismicity distribution.

The Gaussian and extreme-threshold failure models predicts similar spatial distribution of earthquake probability, whether the strain-volume or thin-sheet formulations is chosen to calculate stress redistribution. Slight differences are visible though. For the thin-sheet formulation the Gaussian failure function yields higher probability of failure in the north-west of the reservoir region compared to the extreme-threshold failure criterion.

Contrasting the two stress redistribution models, we observe differences with the strain-volume formulation predicting higher earthquake probabilities localised in the north-west of the reservoir compared to the thin-sheet formulation, with a greater deviation of the maximum probability of failure from the background levels.

5.3. Hindcasting

We investigate here the sensitivity to the duration of training period from the start of the onset of observable seismicity. This allows yo evaluate the amount of data needed to make the forecast consistent with the observations. We test four training periods $1993-1997$, $1993-2001$, $1993-2005$ and $1993-2009$, with the remaining period up to 2017 in each case representing the validation period. For each training period the procedure outline in section 3 is implemented to quantify the earthquake rate from the simulated Coulomb stress models, with the maximum expected magnitude determined from the simulated cumulative number of earthquakes since the start of gas extraction. Figure 10 shows the earthquake rates and maximum expected magnitude for each of the different training periods. If the training period is $1993-1997$ or $1993-2001$, the synthetic earthquake catalogue is unable to match the onset of seismicity. The maximum magnitude is also poorly predicted. For the $1993-2005$ training period, which includes a considerable portion of the rise of earthquake rate, the forecast fits better the observations. The longest training period of $1993-2009$ shows the best agreement between the simulated and observed earthquake rates and maximum magnitude, with a reduced uncertainty in the simulations due to the increased number of earthquakes in the training period.

6. Discussion and Conclusions

This manuscript presents a framework for stress-based earthquake forecasting of induced seismicity which should in principle be applicable in any setting where earthquake are induced by deformation of a reservoir whether due to extraction or injection. The frameworks requires some knowledge of the reservoir geometry and compressibility on one hand, and of the pore pressure evolution on the other hand. By representing the reservoir as a series of poroelastic cuboids, the stress redistribution withing and outside the reservoir can calculated with proper account for stress localization at the faults offsetting the reservoir. The importance of accounting for this process has been demonstrated in a number

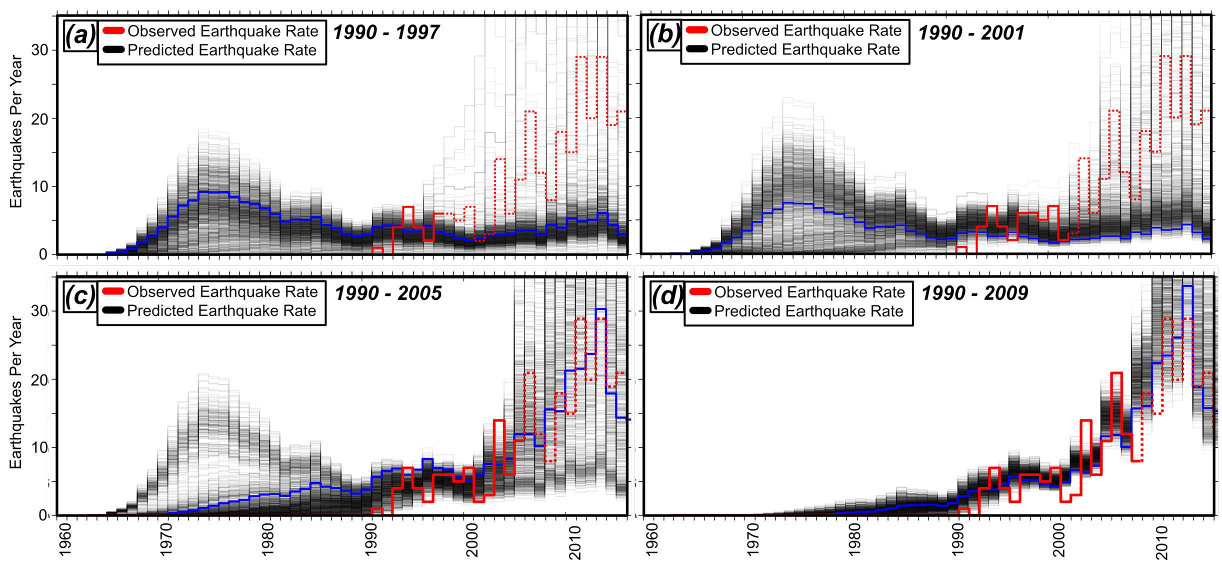

Figure 10: Hindcasting of observed seismicity since 1993. Blue lines represent the maximum a priori estimate of synthetic earthquake rate. Black lines represent samples from the probability distribution with colour dependent on the probability. Red solid line represents the observed seismicity catalogue trained against. Red dashed line represents the observed seismicity catalogue validated against. Pink dashed line represent the magnitude of completeness of the seismicity catalogue. (a) Trained on earthquake rates from $1993-1997$. (b) Trained on earthquake rates from $1993-2001$. (c) Trained on earthquake rates from $1993-2005$. (d) Trained on earthquake rates from $1993-2009$.

of previous studies (Mulders, 2003; Rutqvist et al., 2016; Buijze et al., 2017, 2019; Jansen et al., 2019). In agreement with these studies, we find that the stress changes are at the top or bottom of the reservoir in the vicinity of discontinuities created by faults offsetting the reservoir due to faulting. The model is found consistent with the observation that seismicity hypocenters tend to concentrate in the caprock but does provide any explanation for the lack of a similar concentration in the underburden where stress changes are comparable. It is improbable that earthquake nucleate within the reservoir itself due to the lower Coulomb stress changes resulting from the clamping effect of pore pressure depletion. In this study, the stress changes are calculated using semi-analytical Green functions. This procedure is computationally very efficient and can therefore be applied to compute stress changes at the scale of the entire reservoir over several decades with a sub-kilometric spatial sampling rate and a yearly temporal resolution .

We use our method to calculate stress changes due to the reservoir compaction to feed an earthquake forecasting scheme. Our scheme is similar to but expands on the extreme threshold model of Bourne and Oates (2017); Bourne et al. (2018) by allowing in principle to represent the transition from the initial exponential rise of seismicity to the steady state regime where the seismicity rate should be proportional to the stress rate. We find that the Gaussian failure function, which we introduce to that effect, has in fact an only slightly lower validation loss than the extreme-threshold function. Our results thus suggest that the seismicity at Groningen has actually not yet transitioned to the steady-state regime. Assuming a steady state regime therefore probably lead to an underestimation of the hazard level. We find that the forecasting performance is similar if the stress calculation is based on the elastic thin sheet approximation (Bourne and Oates, 2017) or on the strain-volume method presented here. It is also independent of the chosen vertical distance from the top of the reservoir used to extract the stress changes. This is due to the fact that, in all these cases, the seismicity forecast is driven by the spatial distribution of the discontinuities of the reservoir and the time evolution by the pressure depletion history. The forecasting procedure seems therefore relatively robust to the uncertainty on hypocentral depths. However, it is likely the forecast performance is satisfying because the seismicity has been relatively stationary. If seismicity had shifted to the underburden for example, it is probable that the forecasting performance of the algorithm would drop and that the model parameters would need to be reevaluated. In any case, one should be cautious about the interpretation of the model parameters and about the implications of a satisfying forecast. For example, the stress threshold needed to initiate seismicity in our model depends on the chosen elevation above the reservoir where the stresses are evaluated. A satisfying forecast doesn't mean either that the particular choices made in the stress calculation or the failure functions are correct. As an example a forecast based on the assumption that the earthquakes initiate in the reservoir can be found satisfying, although the assumption is probably incorrect. Similarly, the assumption of a steady regime might seem acceptable to forecast seismicity over a short period of time but the linear extrapolation that the assumption implies could be incorrect and the model parameters (the ratio between the stress rate and the seismicity rate) would be dependent on the period used to calibrate the model and would have little physical significance. The procedures presented in this article is computationally effective and could be implemented into a traffic-light system during reservoir operations. It would also easily allow for data assimilation (re-evaluation of the model parameters as seismicity observations are collected).

In this work we have assumed that earthquakes nucleate instantaneously at a critical stress. We do not account for the finite duration of the nucleation process which can be described using the rate-and-state friction formalism and which has been used in some previous studies and could partly explain the seismicity lag at Groningen (Candela et al., 2019; Richter et al., 2020). These studies use the Dieterich (1994) model, that the earthquake population is at state of steady earthquake production before it is perturbed. This hypothesis therefore ignores that the system may have been initially in a relaxed state due to the low level of tectonic loading in the Groningen context. We therefore didn't test the model as some modification of the formalism, presented in (see Heimisson et al., 2021), is needed to account for a possible initial strength excess. This other study shows that the nucleation process doesn't impact the forecast at the annual to multiannual time scale considered here, but would matter at shorter time scales.

Acknowledgments

This study was supported by the NSF/ IUCRC Geomechanics and Mitigation of Geohazards (National Science Foundation award 1822214). We gratefully acknowledge data and support from Nederlandse Aardoli Maatschappij (Jan Van Elk, Gini Ketellar and Dirk Doornhof), Shell Global Solutions (Stijn Bierman, Steve Oates, Rick Wentinck, Xander Campman, Alexander Droujinine and Chris Harris, and Koninkljjk Nederlands Meteorologisch Instituut (http://www.knmi.nl/). Strain Volume simulations can be found at the interactive Google Colab notebook `https://colab.research.google.com/drive/1GDKMHDO2obj4bT8ezvCxFumHz3CSE3Ns?usp=sharing`.

Contributions

J.D.Smith: Principle lead, Model method conceptualization, software development and manuscript writing. E.R.Heimisson: Model method conceptualization, software development and manuscript writing. S.J.Bourne: Supervision, Model method conceptualization, software development. JP.Avouac: Supervision, Model method conceptualization and manuscript writing.

References

Ader, T.J., Lapusta, N., Avouac, J.P., Ampuero, J.P., 2014. Response of rate-and-state seismogenic faults to harmonic shear-stress perturbations. Geophysical Journal International 198, 385–413.

Bourne, S., Oates, S., Van Elk, J., 2018. The exponential rise of induced seismicity with increasing stress levels in the groningen gas field and its implications for controlling seismic risk. Geophysical Journal International 213, 1693–1700.

Bourne, S.J., Oates, S.J., 2017. Extreme threshold failures within a heterogeneous elastic thin sheet and the spatial-temporal development of induced seismicity within the groningen gas field. Journal of Geophysical Research: Solid Earth 122, 10,299–10,320. URL: `https://agupubs.onlinelibrary.wiley.com/doi/abs/10.1002/2017JB014356`, doi:`10.1002/2017JB014356`, `arXiv:https://agupubs.onlinelibrary.wiley.com/doi/pdf/10.1002/2017JB014356`.

Buijze, L., Van den Bogert, P., Wassing, B., Orlic, B., 2019. Nucleation and arrest of dynamic rupture induced by reservoir depletion. Journal of Geophysical Research: Solid Earth 124, 3620–3645.

Buijze, L., Van Den Bogert, P.A., Wassing, B.B., Orlic, B., Ten Veen, J., 2017. Fault reactivation mechanisms and dynamic rupture modelling of depletion-induced seismic events in a rotliegend gas reservoir. Netherlands Journal of Geosciences 96, s131–s148.

Candela, T., Osinga, S., Ampuero, J.P., Wassing, B., Pluymaekers, M., Fokker, P.A., van Wees, J.D., de Waal, H.A., Muntendam-Bos, A.G., 2019. Depletion-induced seismicity at the groningen gas field: Coulomb rate-and-state models including differential compaction effect. Journal of Geophysical Research: Solid Earth 124, 7081–7104.

Dempsey, D., Suckale, J., 2017. Physics-based forecasting of induced seismicity at groningen gas field, the netherlands. Geophysical Research Letters 44, 7773–7782.

Dieterich, J., 1994. A constitutive law for rate of earthquake production and its application to earthquake clustering. Journal of Geophysical Research: Solid Earth 99, 2601–2618. doi:`https://doi.org/10.1029/93JB02581`.

Dost, B., Ruigrok, E., Spetzler, J., 2017. Development of seismicity and probabilistic hazard assessment for the groningen gas field. Netherlands Journal of Geosciences 96, s235–s245.

Dost, B., van Stiphout, A., Kühn, D., Kortekaas, M., Ruigrok, E., Heimann, S., 2020. Probabilistic moment tensor inversion for hydrocarbon-induced seismicity in the groningen gas field, the netherlands, part 2: Application. Bulletin of the Seismological Society of America 110, 2112–2123.

Handin, J., 1969. On the coulomb-mohr failure criterion. Journal of Geophysical Research 74, 5343–5348.

Heimisson, E.R., Smith, J.D., Avouac, J.P., Bourne, S., 2021. Coulomb threshold rate-and-state model for fault reactivation: Application to induced seismicity at Groningen doi:https://doi.org/10.31223/X5489T.

Jansen, J., Singhal, P., Vossepoel, F., 2019. Insights from closed-form expressions for injection-and production-induced stresses in displaced faults. Journal of Geophysical Research: Solid Earth 124, 7193–7212.

King, G.C., Stein, R.S., Lin, J., 1994. Static stress changes and the triggering of earthquakes. Bulletin of the Seismological Society of America 84, 935–953.

Kuvshinov, B.N., 2008. Elastic and piezoelectric fields due to polyhedral inclusions. International Journal of Solids and Structures 45, 1352–1384.

Langenbruch, C., Shapiro, S.A., 2014. Gutenberg-richter relation originates from coulomb stress fluctuations caused by elastic rock heterogeneity. Journal of Geophysical Research: Solid Earth 119, 1220–1234. URL: https://agupubs.onlinelibrary.wiley.com/doi/abs/10.1002/2013JB010282, doi:https://doi.org/10.1002/2013JB010282, arXiv:https://agupubs.onlinelibrary.wiley.com/doi/pdf/10.1002/2013JB010282.

van der Molen, J., Peters, E., Jedari-Eyvazi, F., van Gessel, S.F., 2019. Dual hydrocarbon–geothermal energy exploitation: potential synergy between the production of natural gas and warm water from the subsurface. Netherlands Journal of Geosciences 98.

Mulders, F.M.M., 2003. Modelling of stress development and fault slip in and around a producing gas reservoir. Doctoral Thesis .

Nederlandse Aardolie Maatschappij, 2013. A technical addendum to the winningsplan groningen 2013 subsidence, induced earthquakes and seismic hazard analysis in the groningen field. NAM, Assen .

Ogata, Y., 1998. Space-time point-process models for earthquake occurrences. Annals of the Institute of Statistical Mathematics 50, 379–402. doi:10.1023/A:1003403601725.

Richter, G., Sebastian, H., Torsten, D., Gert, Z., 2020. Stress-based, statistical modeling of the induced seismicity at the groningen gas field, the netherlands. Environmental Earth Sciences 79.

Rutqvist, J., Rinaldi, A.P., Cappa, F., Jeanne, P., Mazzoldi, A., Urpi, L., Guglielmi, Y., Vilarrasa, V., 2016. Fault activation and induced seismicity in geological carbon storage–lessons learned from recent modeling studies. Journal of Rock Mechanics and Geotechnical Engineering 8, 789–804.

Smith, J.D., Avouac, J.P., White, R.S., Copley, A., Gualandi, A., Bourne, S., 2019. Reconciling the long-term relationship between reservoir pore pressure depletion and compaction in the groningen region. Journal of Geophysical Research: Solid Earth 124, 6165–6178. URL: https://agupubs.onlinelibrary.wiley.com/doi/abs/10.1029/2018JB016801, doi:10.1029/2018JB016801, arXiv:https://agupubs.onlinelibrary.wiley.com/doi/pdf/10.1029/2018JB016801.

Smith, J.D., White, R.S., Avouac, J.P., Bourne, S., 2020. Probabilistic earthquake locations of induced seismicity in the groningen region, the netherlands. Geophysical Journal International 222, 507–516.

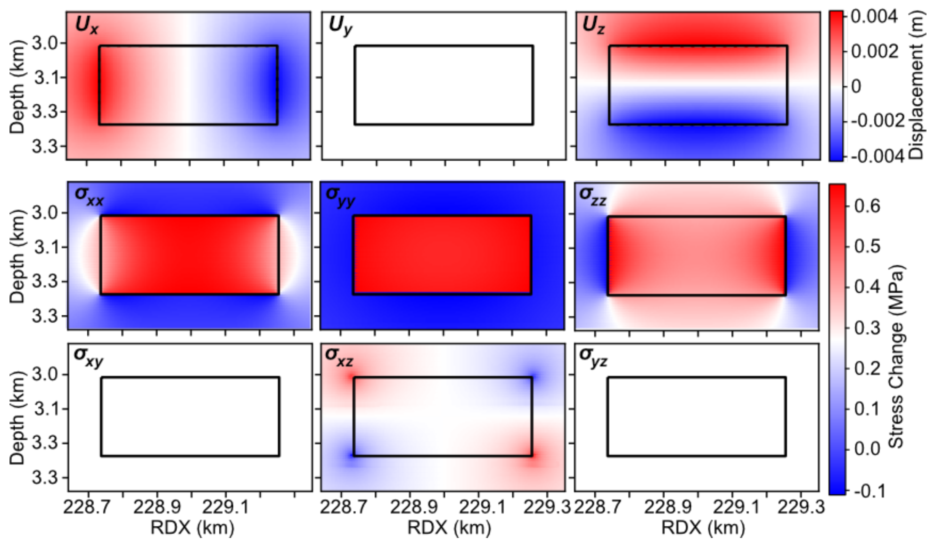

Figure A1: Displacement and stress changes induced by a single cuboid. The position and width of the cuboid is $[228.5 \text{ km RDX}, 574.5 \text{ km RDX}, 3.018 \text{ km Depth}]$ and $[500 \text{ m}, 500 \text{ m}, 216 \text{ m}]$. The pressure depletion and uniaxial compressibility is 3.3 MPa and 1.816×10^{-11}

Wang, H., 2018. Introduction to poroelasticity .

van Wees, J.D., Pluymaekers, M., Osinga, S., Fokker, P., Van Thienen-Visser, K., Orlic, B., Wassing, B., Hegen, D., Candela, T., 2019. 3-d mechanical analysis of complex reservoirs: a novel mesh-free approach. Geophysical Journal International 219, 1118–1130.

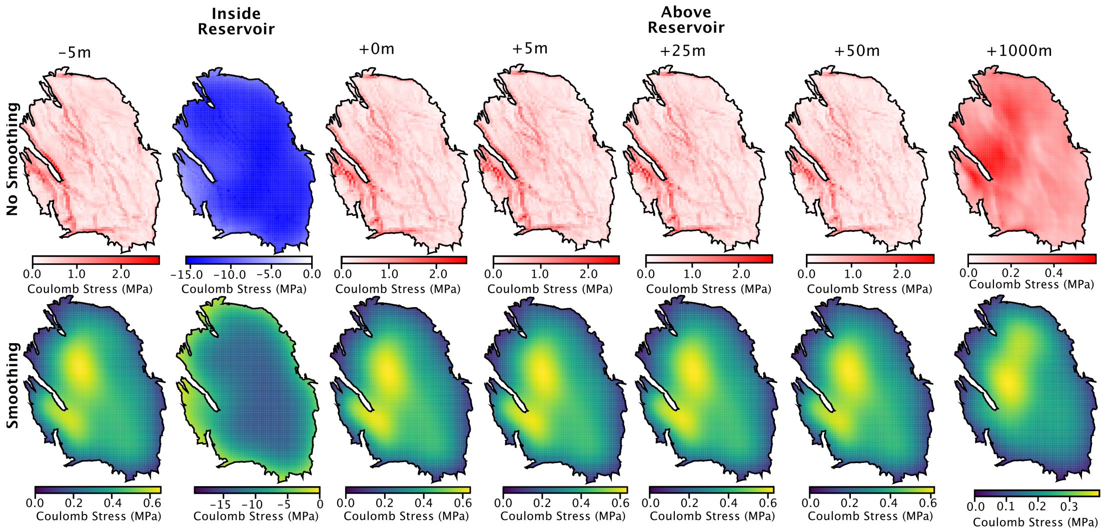

Figure A2: Maximum Coulomb Stress redistribution at different depths. Top row represents the non-smoothed Coulomb stress change. Bottom row represents the smoothed Coulomb stress to $3km$, that of the minimum resolvable dataset. Columns represent the different depth slices relative to the reservoir.

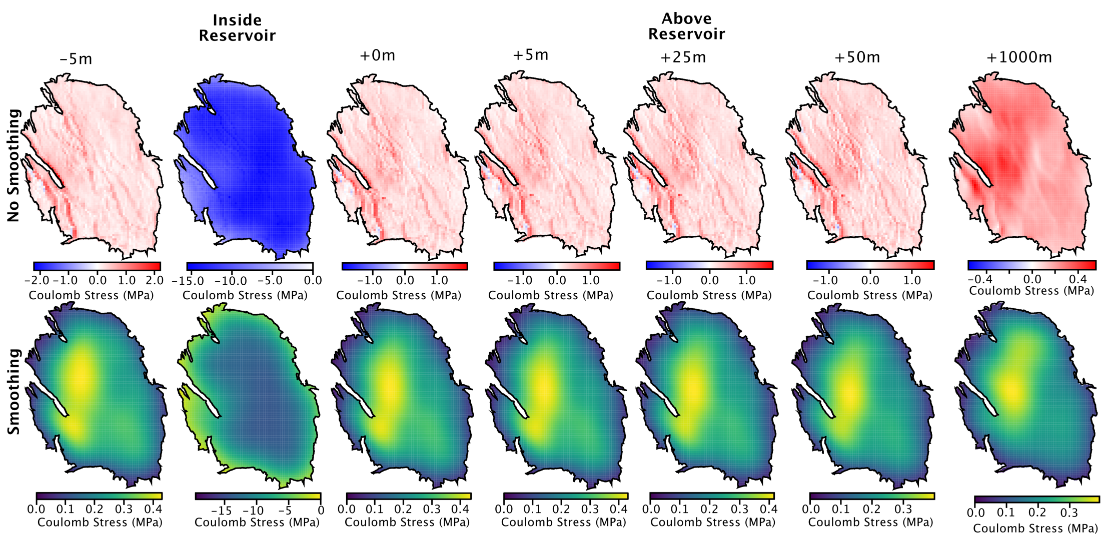

Figure A3: Fault Coulomb Stress redistribution at different depths. Top row represents the non-smoothed Coulomb stress change. Bottom row represents the smoothed Coulomb stress to $3km$, that of the minimum resolvable dataset. Columns represent the different depth slices relative to the reservoir

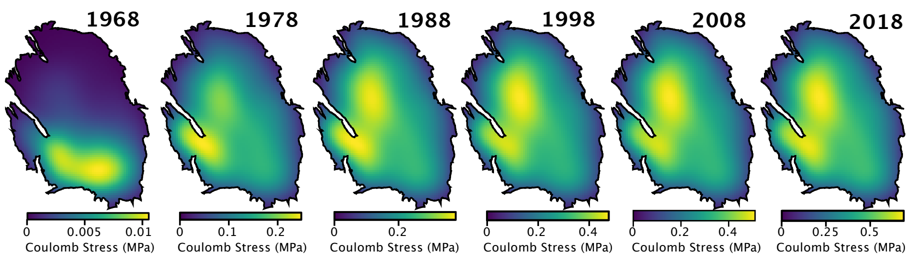

Figure A4: Time evolution of reservoir maximum Coulomb stress change for a slice taken 5m above the top of the reservoir.

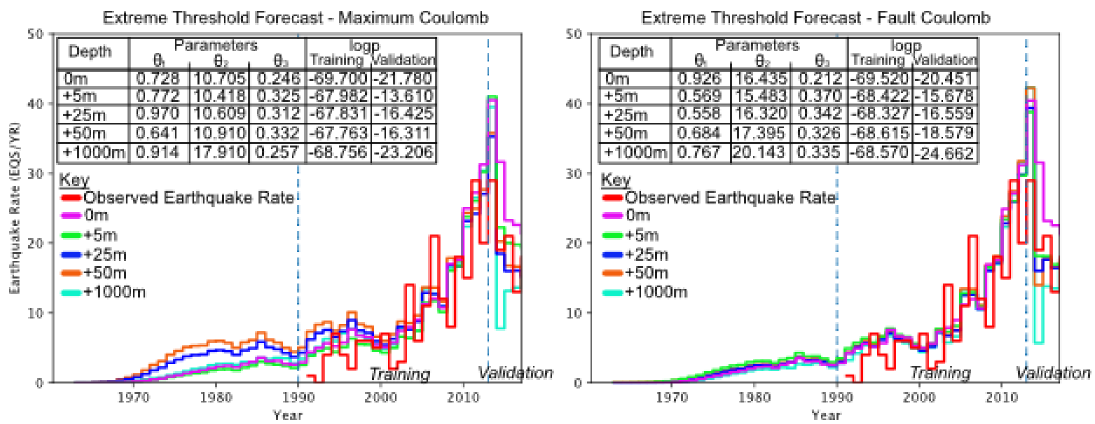

Figure A5: Earthquake Rates at different depths using the Extreme Threshold Failure Criterion for both the Maximum and Fault derived Coulomb stress.

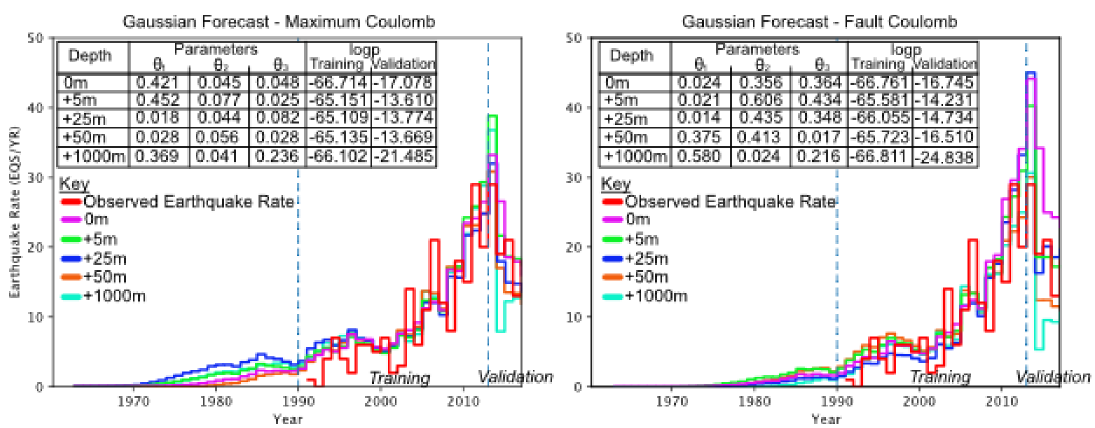

Figure A6: Earthquake Rates at different depths using the Gaussian Failure Criterion for both the Maximum and Fault derived Coulomb stress.